

Article

Visible-Light Active and Magnetically Recyclable Nanocomposites for the Degradation of Organic Dye

Helin Niu ^{1,*} Qinmin Wang ¹, Hongxia Liang ¹, Min Chen ², Changjie Mao ¹, Jiming Song ¹, Shengyi Zhang ¹, Yuanhao Gao ³ and Changle Chen ^{2,*}

¹ Anhui Province Key Laboratory of Environment-friendly Polymer Materials, School of Chemistry and Chemical Engineering, Anhui University, Hefei 230601, Anhui, China; E-Mails: qinminwang12@gmail.com (Q.W.); hongxia828@gmail.com (H.L.); maocj2011@gmail.com (C.M.); songjm@ustc.edu.cn (J.S.); syzhangj@126.com (S.Z.)

² CAS Key Laboratory of Soft Matter Chemistry, Department of Polymer Science and Engineering, University of Science and Technology of China, Hefei 230026, Anhui, China; E-Mail: misschen@mail.ustc.edu.cn

³ School of Chemistry and Chemical Engineering, Xuchang University, Xuchang 461000, Henan, China; E-Mail: yuanhaogao2@gmail.com

* Authors to whom correspondence should be addressed; E-Mails: niuhelin@ahu.edu.cn (H.N.); changle@ustc.edu.cn (C.C.).

Received: 2 April 2014 / in revised form: 7 May 2014 / Accepted: 13 May 2014 /

Published: 21 May 2014

Abstract: Recyclable visible-light photocatalyst Fe₃O₄@TiO₂ with core-shell structure was prepared by a simple synthetic strategy using solvothermal crystallization of titanium precursor on preformed Fe₃O₄ nanoparticles. The photo-degradation reaction of neutral red aqueous solution was tested to evaluate the visible-light photocatalytic activity of the as prepared Fe₃O₄@TiO₂ nanoparticles, which show excellent photocatalytic activity compared with commercial P25 catalyst. Moreover, the Fe₃O₄@TiO₂ nanocomposites can be easily separated from the reaction mixture, and maintain favorable photocatalytic activity after five cycles. The high visible light absorption of the Fe₃O₄@TiO₂ nanocomposites may originate from the absence of electronic heterojunction, excellently dispersity and the high specific surface area of the as-synthesized Fe₃O₄@TiO₂ samples.

Keywords: magnetic photocatalysts; synthesis; TiO₂; visible-light irradiation

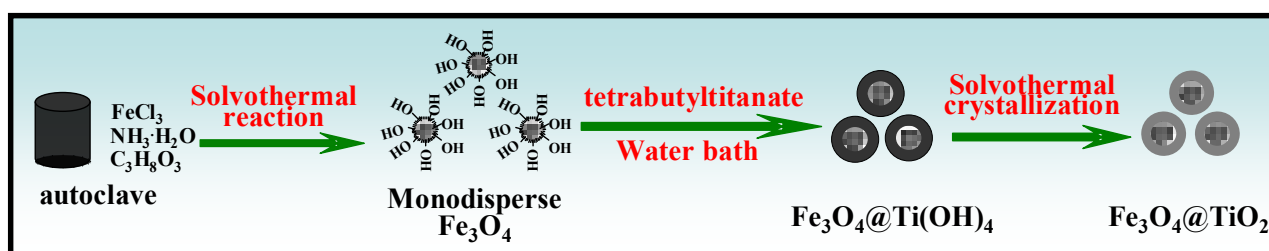
1. Introduction

Pollutions of commercial dyes have become one of the most serious environmental issues. Recently, photo-catalysis using sunlight has emerged as one of the most attractive techniques for various environmental applications such as wastewater treatment. As the most commonly used photo-catalyst, TiO_2 has been extensively studied for the detoxification of wastewater [1,2]. However, its large-scale application has been limited due to the following disadvantages: (1) The large band gap ($E_g = 3.2$ eV) means it can only be excited by ultraviolet (UV) light, which is only about 4% of solar spectrum [3]; (2) The low barrier for the recombination of photogenerated electron-hole pairs reduces the quantum efficiency and the photo-catalytic activity [4]. Extensive efforts have been made to develop TiO_2 photo-catalysts that can more efficiently utilize solar or indoor light. Some reports have demonstrated that the introduction of nonmetal [5–8], lanthanide ions [9,10], transitional metal ions [11–13], noble metals [14] and metallic oxides [15] into TiO_2 lattice can reduce the recombination of electron-hole pairs and enhance its absorption in visible region. However, there have been very few examples about the photocatalyst possessing both visible-light activity and magnetic properties.

Core-shell structured materials combine the properties of two or several materials by synergistic effect, which may lead to unique properties. $\text{Fe}_3\text{O}_4@/\text{TiO}_2$ composite system has attracted a lot of attention due to its magnetic property. However, most of the previously reported $\text{Fe}_3\text{O}_4@/\text{TiO}_2$ systems suffer from dramatically reduced photocatalytic activities due to the electron-hole recombination resulting from the electronic heterojunction between the core-shell $\text{Fe}_3\text{O}_4@/\text{TiO}_2$ structures [16,17]. An alternative strategy was developed to solve this issue by coating the Fe_3O_4 core with SiO_2 insulation layer to avoid unfavorable heterojunction and photodissolution. However, the high temperature (around 500 °C) treatment required during the synthesis usually led to the loss of magnetism, change of iron oxide phase or the generation of mixed iron/titanium oxide [18–23]. Moreover, most of these composite systems only respond to UV light irradiation [24–26]. The development of both magnetically and photocatalytically active catalyst systems is very challenging.

Herein, we report a novel synthetic route for the preparation of recyclable Visible-light photocatalyst $\text{Fe}_3\text{O}_4@/\text{TiO}_2$ under relatively low temperature (Scheme 1). The method leads to excellently dispersed and homogeneous nanoparticles by avoiding the growing and reuniting of powders. Due to the low synthetic temperature, the magnetic properties and photocatalytic activity of the composites do not deteriorate [27]. The as-prepared materials have higher visible-light absorption and much higher photo-catalytic activity in neutral red decomposition reaction comparing with commercial P25 and can be easily separated and recycled by simple utilization of a magnetic bar.

Scheme 1. Synthetic route to $\text{Fe}_3\text{O}_4@/\text{TiO}_2$ core-shell nanocomposites.



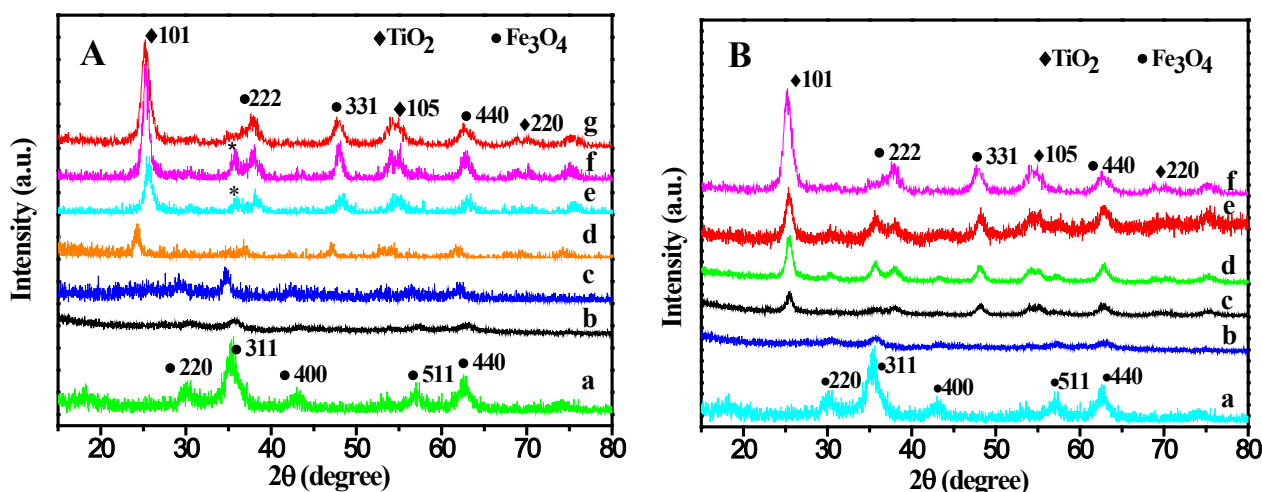
2. Results and Discussion

The XRD patterns of the Fe_3O_4 and $\text{Fe}_3\text{O}_4@\text{TiO}_2$ nanocomposites prepared under different temperature and different time were shown in Figures 1A,B, which showed that the as prepared samples are of high purity. The samples were scanned from 20° to 80° , 2θ degrees using a $\text{Cu K}\alpha$ radiation with a characteristic wavelength (λ) of 0.15405 nm. The Fe_3O_4 nanoparticles exhibit a broad peak at about $2\theta = 35.2^\circ$ (Figure 1A,B), which is the (311) reflection and has highly crystalline cubic spinel structure, agreeing well with the standard Fe_3O_4 XRD spectrum (JCPDS card No. 89-3854). Figures 1A-b and 2B-b are the XRD patterns of predecessor of $\text{Fe}_3\text{O}_4@\text{TiO}_2$. The weak diffraction peaks of Fe_3O_4 were observed. The diffraction peaks of TiO_2 are stronger and broader with the increasing of the reaction temperature from Figure 1A(c–g) and the reaction time from Figure 1B(c–f). These peaks can be attributed to (101), (105) and (220) reflections of anatase TiO_2 , agreeing well with the standard anatase TiO_2 XRD spectrum (JCPDS card No. 89-4203). The iron compound peaks in the XRD patterns became weaker and weaker, due to the formation of the TiO_2 shell on the surface of iron oxide. Scherrer method was used to determine the grain size Scherrer based on the (101), (331) and (440) reflection equation as follows [28]:

$$D = K\lambda/\beta\cos\theta \quad (1)$$

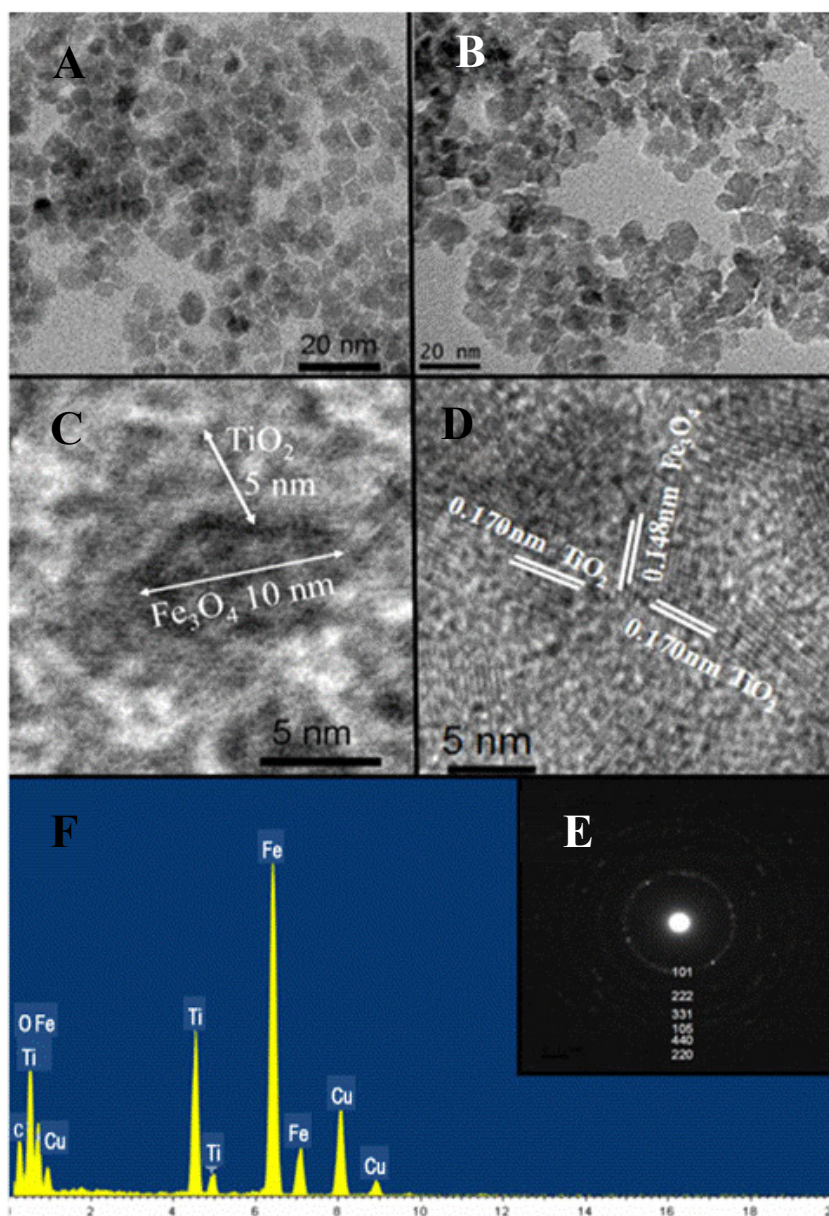
where D is the average diameter of the calculated particles; K is the shape factor of the average grain size (the expected shape factor is 0.89); λ is the wavelength characteristic in \AA (in this particular case $\lambda = 1.5405 \text{ \AA}$); β is the width of the X-ray peak at half its high. The average crystallites size of $\text{Fe}_3\text{O}_4@\text{SiO}_2$ prepared at different temperatures of 200°C , 175°C , 150°C and 135°C are 18.6 nm, 22.4 nm and 22.8 nm and 24.8 nm. The average crystallites size of $\text{Fe}_3\text{O}_4@\text{SiO}_2$ prepared at different times at 10 h, 8 h, 6 h, 4 h are 18.6 nm, 19.1 nm, 22.1 nm and 22.6 nm. High temperature and long reaction time lead to smaller crystallites. Based on the XRD spectrum analysis, the optimal solvothermal crystallization condition is 200°C and 8 h.

Figure 1. (A) XRD spectra of different samples of (a) Fe_3O_4 and $\text{Fe}_3\text{O}_4@\text{TiO}_2$ of prepared at different temperatures of (b) 0°C , (c) 100°C , (d) 125°C , (e) 150°C , (f) 175°C , (g) 200°C ; (B) XRD spectra of different samples of (a) Fe_3O_4 and $\text{Fe}_3\text{O}_4@\text{TiO}_2$ of prepared at different time under 200°C of (b) 0 h, (c) 4 h, (d) 6 h, (e) 8 h, (f) 10 h.



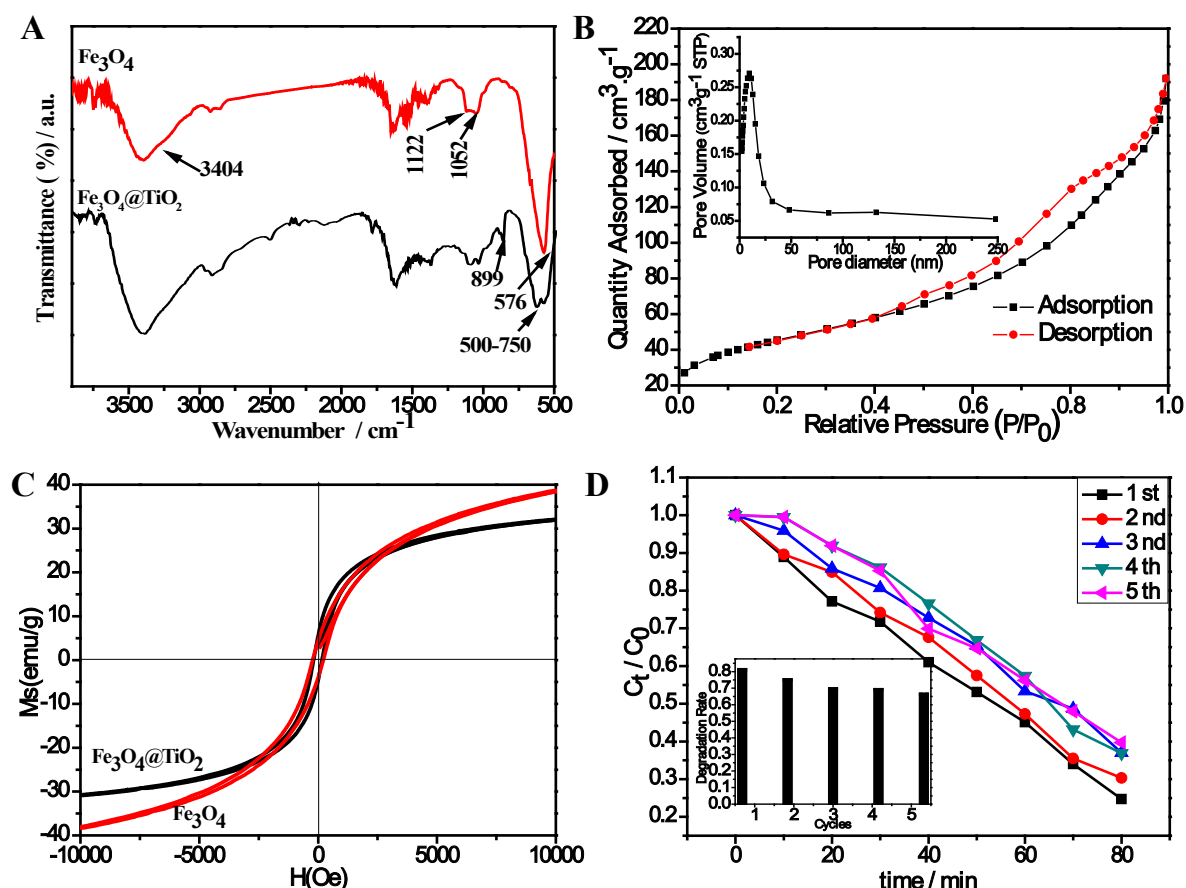
TEM image of the Fe_3O_4 nanoparticles shows excellent monodispersity with an average diameter of 10 nm (Figure 2A). TEM images of the $\text{Fe}_3\text{O}_4@ \text{TiO}_2$ nanocomposites indicate an average diameter of 20 nm and a typical core-shell structure (Figure 2B,C). The thickness for the black core (Fe_3O_4) and shell (TiO_2) is *ca.* 10 nm and 5 nm. HRTEM analysis shows highly crystalline structure with lattice space of 0.148 nm and 0.17 nm, corresponding to the (440) plane for Fe_3O_4 and (105) plane for TiO_2 (Figure 2D). SAED pattern (Figure 2E) shows a twinned structure with six diffraction rings originating from the TiO_2 (101), (105), (220) planes and the Fe_3O_4 (222), (331), (440) planes, which agrees very well with the XRD patterns. The EDX analysis (Figure 2F) reveals the existence of Fe, Ti, O, C and Cu elements with atomic percentage of 23.46, 10.25, 33.37, 26.13, 6.79, in which C and Cu were from a copper grid with carbon film. The iron peak is weak due to the shielding of the TiO_2 shell.

Figure 2. TEM images of (A) the synthesized Fe_3O_4 nanocomposites; (B,C) $\text{Fe}_3\text{O}_4@ \text{TiO}_2$ core-shell nanocomposites synthesized by solvothermal crystallization method; (D–F) HRTEM, SAED and EDX spectrum of $\text{Fe}_3\text{O}_4@ \text{TiO}_2$ core-shell nanocomposites.



The FT-IR spectrum of the Fe_3O_4 nanoparticles (Figure 3A) shows a characteristic band for Fe–O stretching vibration at 576 cm^{-1} [29], the broad bands at *ca.* 3400 cm^{-1} and 1100 cm^{-1} are associated with the O–H stretching and bending vibration [30,31]. These results suggested that the Fe_3O_4 surfaces are linked with hydroxyl groups, which not only enables better dispersity of the Fe_3O_4 nanoparticles, but also enhances the affinity between the Fe_3O_4 nanoparticles and the predecessor TiO_2 . The FT-IR spectrum of the $\text{Fe}_3\text{O}_4@\text{SiO}_2$ nanoparticles (Figure 3A) shows characteristic absorption peaks at $500\text{--}750\text{ cm}^{-1}$ of titania [29], further confirming the successful preparation of the $\text{Fe}_3\text{O}_4@\text{TiO}_2$ microspheres. Nitrogen adsorption and desorption isotherms were used to investigate the specific surface area and porosity of the as-prepared $\text{Fe}_3\text{O}_4@\text{TiO}_2$ nanomaterials, and the corresponding N_2 adsorption-desorption isotherms and pore size distributions are shown in Figure 3B. It can be seen that the samples have type IV isotherms (according to IUPAC classification) [27]. The Brunauer–Emmett–Teller (BET) specific surface area of the as-synthesized $\text{Fe}_3\text{O}_4@\text{TiO}_2$ samples is $160.474\text{ m}^2\cdot\text{g}^{-1}$ by calculation from nitrogen adsorption. The single point adsorption total pore volume of pores is less than 501.4597 nm diameter. The high specific surface area of the sample nanostructures may provide more active sites for the catalytic reaction.

Figure 3. (A) FT-IR spectra of the as-made Fe_3O_4 nanoparticles (a) and $\text{Fe}_3\text{O}_4@\text{SiO}_2$ nanoparticles (b); (B) N_2 adsorption and desorption isotherms and pore-size distribution (inset) of the $\text{Fe}_3\text{O}_4@\text{TiO}_2$; (C) M-H curves at room temperature of $\text{Fe}_3\text{O}_4@\text{TiO}_2$ and Fe_3O_4 . The insert is the magnetic separation photographs of $\text{Fe}_3\text{O}_4@\text{TiO}_2$; (D) UV-Vis absorption spectrum of the P25 and $\text{Fe}_3\text{O}_4@\text{TiO}_2$ and the Kulbeka-Munk plot of the energy band gap.



The magnetic behavior of $\text{Fe}_3\text{O}_4@\text{TiO}_2$ and Fe_3O_4 are investigated using M-H curves from VSM analysis at room temperature (Figure 3C). The saturation magnetization value (M_s), coercivity (H_c), remanent magnetization (M_r) of $\text{Fe}_3\text{O}_4@\text{TiO}_2$ nanocomposites are 30.75 emu/g, 167.89 Oe and 6.14 emu/g, respectively. In contrast, the M_s , H_c and M_r values of the Fe_3O_4 are 38.55 emu/g, 229.34 Oe and 4.6 emu/g, respectively. This may be due to the lower content of Fe_3O_4 in $\text{Fe}_3\text{O}_4@\text{TiO}_2$. The $\text{Fe}_3\text{O}_4@\text{TiO}_2$ sample is still considered to be superparamagnetic due to its small H_c and M_r value though individual particles may be larger than the superparamagnetic critical size (20 nm) [32]. From the insert in Figure 3C, it can be seen that as prepared $\text{Fe}_3\text{O}_4@\text{TiO}_2$ nanocomposites can be evenly dispersed in water, and easily separated from water upon placing a small magnetic bar at one side of the bottle.

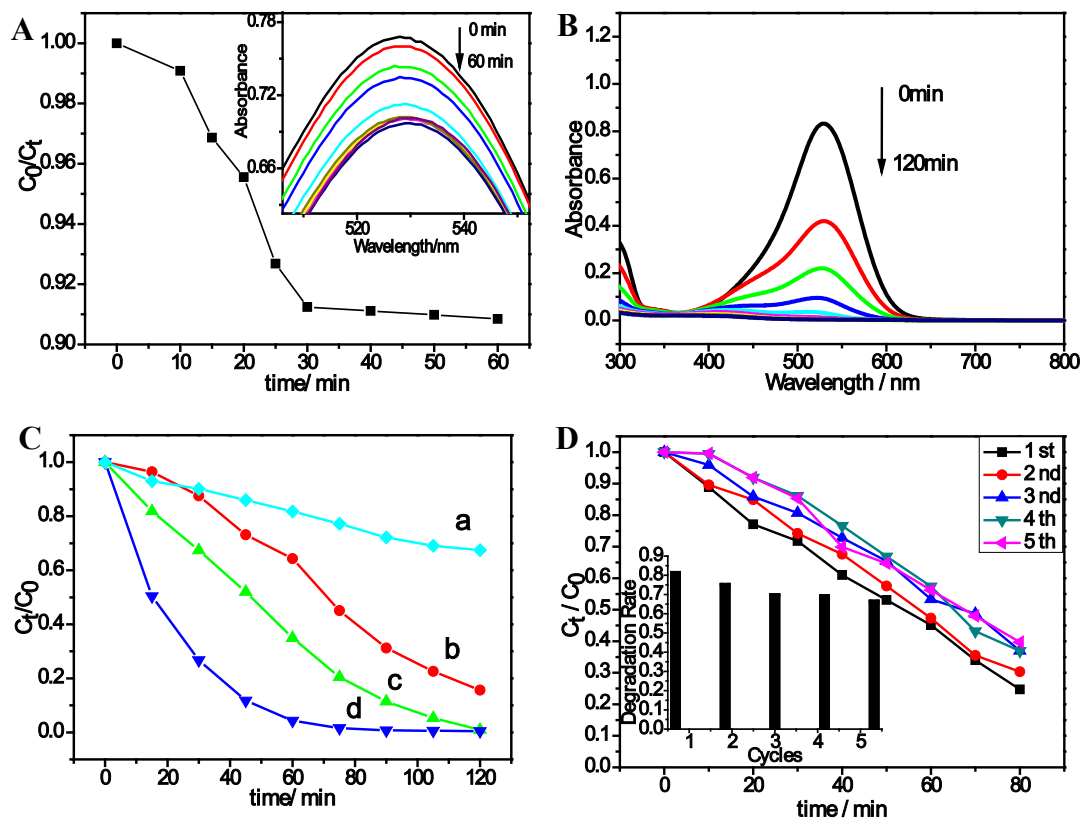
$\text{Fe}_3\text{O}_4@\text{TiO}_2$ has a broad absorption (200–800 nm) in UV-Vis analysis (Figure 3D). In contrast, commercial P25 shows minimum absorption in the >400 nm range. The energy band gap of the samples as a semiconductor was calculated by the Kubelka-Munk theory [33]. The relationship between absorption coefficient (α) and the incident photon energy ($h\nu$) can be written as $\alpha = B_d (h\nu - E_g)^{1/2}/(h\nu)$, where B_d is the absorption constant. The Kubelka-Munk plot of $(\alpha h\nu)^{1/2}$ versus $(h\nu)$ was presented in the insert. The extrapolated value of the absorption edge was about 2.10 eV. This value is much narrower than pure TiO_2 (3.2 eV). The significant absorption in the >400 nm range and the small band gap suggested its possible photocatalytic properties under visible light.

The photocatalytic properties of $\text{Fe}_3\text{O}_4@\text{TiO}_2$ composite were investigated with the degradation reaction of neutral red in aqueous solution under 400–700 nm wavelength to mimic sunlight. Figure 4B shows the UV-Vis absorbance peak of neutral red (at 530 nm) [34] gradually decreased with irradiation time and completely disappeared after the reaction. Figure 4A shows that the absorbance of the neutral red solution decreases with the time in the dark. After 30 min, there is no obvious change in absorbance, indicating that equilibrium is reached. Figure 4C shows the concentration profiles of neutral red during the experiment. The degradation is very slow in the presence of only dye and light (without catalyst, Figure 4C(a)). The activity of $\text{Fe}_3\text{O}_4@\text{TiO}_2$ (Figure 4C(d)) is much higher than that of the commercial catalyst P25 (Figure 4C-d). This is not surprising since $\text{Fe}_3\text{O}_4@\text{TiO}_2$ demonstrates significant absorption in the visible light region while P25 does not (Figure 3D).

The surprising visible light absorption and the excellent visible light photocatalytic activity might originate from the absence of electronic heterojunction, excellent dispersity and the high specific surface area of the $\text{Fe}_3\text{O}_4@\text{TiO}_2$ structures. In contrast, Sample-2 was prepared under the same conditions except 10 mL distilled water was used instead of 10 mL urea solution. Sample-2 has much lower activity than P25 or $\text{Fe}_3\text{O}_4@\text{TiO}_2$ composites, suggesting the crucial role of the urea. The presence of urea during the synthesis may which may introduce N-doping in the $\text{Fe}_3\text{O}_4@\text{TiO}_2$ composites. It has been shown before that N-doping in TiO_2 can induce visible light adsorption [35–37].

Recyclability experiment was also studied (Figure 4D). After each experiment, the photocatalysts were separated by applying an external magnetic field, washed three times with ethanol, dried at 60 °C and redistributed in fresh neutral red solution. The catalyst showed favorable reusability after five times of recycling. We did observe some extent of the loss in the catalytic activity after each cycle. The decrease in the degradation rate may be due to the weakening of the absorbance ability of the catalysts or the loss of some catalysts during the collection.

Figure 4. (A) The adsorption rate curves of neutral red test in the dark with the presence of $\text{Fe}_3\text{O}_4@\text{TiO}_2$. The insert is the adsorption curves of neutral red in the dark with the presence of $\text{Fe}_3\text{O}_4@\text{TiO}_2$ nanocomposites; (B) the photodegradation curves of neutral red under visible light in the presence of $\text{Fe}_3\text{O}_4@\text{TiO}_2$ nanocomposites; (C) the photodegradation rate curves of neutral red test in presence of only visible light without catalyst (a) and under the visible light irradiation with Sample-2 (b), P25 (c) and $\text{Fe}_3\text{O}_4@\text{TiO}_2$ nanocomposites (d); (D) the degradation rate of the neutral red by $\text{Fe}_3\text{O}_4@\text{TiO}_2$ nanocomposites. The insert is the normalized rate constant in different cycles



3. Experimental Section

3.1. Materials

Anhydrous FeCl_3 , ammonia, glycerol, tetrabutyl titanate (TBOT), polyvinylpyrrolidone (PVP), urea, absolute ethanol ($\text{C}_2\text{H}_5\text{OH}$). All chemicals are of analytical grade and used without any purification; Deionized water was used throughout the experiments.

3.2. Synthesis

Scheme 1 shows the synthetic route to $\text{Fe}_3\text{O}_4@\text{TiO}_2$ core-shell nanocomposites. 0.16 g anhydrous FeCl_3 was fully dispersed in 5 mL ammonia. Fifteen mL glycerol was added to the above mixture, which was transferred into a Teflon-sealed autoclave. The autoclave was heated at 180°C for 10 h before being cooled in air naturally. The magnetic Fe_3O_4 nanoparticles were separated by a magnet and washed three times by distilled water and redispersed in 10 mL absolute ethanol for subsequent

processing. Under mechanical stirring, tetrabutyl titanate (TBOT) was diluted in absolute ethanol containing 0.08 g PVP and added to the Fe_3O_4 suspension. The mixture was sufficiently mixed and heated in water bath at 80 °C for 15 h. During this process, a mixture of 20 mL ethanol and 10 mL urea were added dropwise. Then, the suspension was aged for 12 h so that $\text{Ti}(\text{OH})_4$ can adsorb on the surface of the Fe_3O_4 nanoparticles. The composite particles were aggregated by an external magnetic field, and washed three times with distilled water and absolute ethanol. The magnetic particles were resuspended in a proper amount of absolute ethanol and the solution was transferred into a Teflon-sealed autoclave. The autoclave was heated to 200 °C for 8 h, and dark brown magnetic nanocomposites were obtained. The final $\text{Fe}_3\text{O}_4@\text{TiO}_2$ core-shell nanocomposites were separated by magnet, washed three times by ethanol and oven-dried at 60 °C for 4 h. Another $\text{Fe}_3\text{O}_4@\text{TiO}_2$ core-shell nanocomposites were synthesized by the same method except 10 mL distilled water was used instead of 10 mL urea solution and designated as Sample-2.

3.3. Evaluation Photocatalytic Activity

The photocatalytic activity was evaluated by the degradation of neutral red aqueous solution at room temperature. Twenty mg catalysts were suspended in 70 mL dye solution ($10 \text{ mg}\cdot\text{L}^{-1}$). The solution was continuously stirred in the dark for 30 min. Then, the solution was exposed to visible light from a 30 W xenon lamp (PLS-SXE 300, Beijing, China, and the UV light was filtered by the filter). The water samples were collected by magnetic field every 15 min to measure the concentration of dye solution with UV-Vis spectra. After the reaction, the magnetic catalysts were collected using a permanent magnetic field, washed with ethanol for 3 times, dried in oven at 60 °C for 4 h, and rested for the recyclability experiment. The concentration change (C/C_0) and the percent conversion ($(C-C_0)/C_0$) of the dye were calculated and plotted vs. irradiation time.

3.4. Characterization

X-ray powder diffraction (XRD) of Fe_3O_4 and $\text{Fe}_3\text{O}_4@\text{TiO}_2$ core-shell nanocomposites were obtained using X-ray diffractometry (XRD, Rigaku D/max-RA, graphite monochromatized $\text{CuK}\alpha$ radiation, $\lambda = 1.5406 \text{ \AA}$, at 36 kV and 25 mA). Transmission electron microscopy (TEM), High resolution transmission electron microscopy (HRTEM) and energy-dispersive X-ray (EDX) analysis were obtained by a JEM-2100 transmission electron microscope (accelerating voltage = 200 kV). IR spectra were measured by using KBr pellets on a NECUS-870. The ultraviolet-visible (UV-Vis) diffuse reflectance spectroscopy and the UV-Vis absorption of the products were recorded on a UV spectrometer (UV-1750). Magnetic properties of samples were evaluated on a BHV-55 vibrating sample magnetometer (VSM).

4. Conclusions

In summary, Recyclable visible-light active photocatalyst $\text{Fe}_3\text{O}_4@\text{TiO}_2$ with core-shell structure was prepared by a simple synthetic method under mild conditions. The as-prepared nanocomposites were characterized by XRD, TEM, UV-Vis and magnetic analysis, which showed great dispersity, high crystallinity and good magnetic property. Very surprisingly, the nanocomposites demonstrate

significant absorption in the Visible light region and is much more active than commercial P25 in the neutral red decomposition reaction. More importantly, the photocatalyst can be easily separated by an external magnetic field and reused. After five cycles, the catalyst still maintained great catalytic activities. This method provides a simple while general strategy to improve the photocatalytic properties of TiO₂ under Visible light, and introduces magnetic properties at the same time.

Acknowledgments

This work was supported by the National Natural Science Foundation of China (Grant Nos. 21071002, 21275006, 21271152 and 21374108), Anhui Provincial Natural Science Foundation (1408085QB28), Key Project of Anhui Provincial Education Department (KJ2013A029), 211 project of Anhui University and Recruitment Program of Global Experts.

Author Contributions

Qinmin Wang, Hongxia Liang, Min Chen, Changjie Mao, Jiming Song, Shengyi Zhang and Yuanhao Gao performed the preparation of the samples, the characterizations and the catalytic studies. Helin Niu and Changle Chen conceived and supervised the project. Helin Niu and Changle Chen wrote the manuscript with contributions from all authors.

Conflicts of Interest

The authors declare no conflict of interest.

References

1. Kleiman, A.; Marquez, A.; Lamas, D.G. Anatase TiO₂ films obtained by cathodic arc deposition. *Surf. Coat. Technol.* **2007**, *201*, 6358–6362.
2. Behnajady, M.A.; Modirshahla, N.; Daneshvar, N.; Rabbani, M. Photocatalytic degradation of an azo dye in a tubular continuous-flow photoreactor with immobilized TiO₂ on glass plates. *Chem. Eng. J.* **2007**, *127*, 167–176.
3. Nguyen, V.N.H.; Amal, R.; Beydoun, D. Photodeposition of CdSe using Se-TiO₂ suspensions as photocatalysts. *J. Photoch. Photobio. A* **2006**, *179*, 57–65.
4. Chen, J.Y.; Qian, Y.; Wei, X.Z. Comparison of magnetic-nanometer titanium dioxide/ferriferous oxide (TiO₂/Fe₃O₄) composite photocatalyst prepared by acid-sol and homogeneous precipitation methods. *J. Mater. Sci.* **2010**, *45*, 6018–6024.
5. Xu, Y.J.; Zhuang, Y.; Fu, X. New insight for enhanced photocatalytic activity of TiO₂ by doping carbon nanotubes: A case study on degradation of benzene and methyl orange. *J. Phys. Chem. C* **2010**, *114*, 2669–2676.
6. Choi, Y.; Mebayashi, T.; Yoshikawa, U.M. Fabrication and characterization of C-doped anatase TiO₂ photocatalysts. *J. Mater. Sci.* **2004**, *39*, 1834–1839.
7. Wang, D.H.; Jia, L.; Wu, X.L.; Lu, L.Q. One-step hydrothermal synthesis of N-doped TiO₂/C nanocomposites with high visible light photocatalytic activity. *Nanoscale* **2012**, *4*, 576–584.

8. Dunnill, C.W.; Parkin, I.D. Silver enhanced TiO₂ thin films: Photocatalytic characterization using aqueous solutions of tris (hydroxymethyl) aminomethane. *Dalton Trans.* **2011**, *40*, 1635–1640.
9. Luo, W.Q.; Li, R.F.; Liu, Y.S.; Zhu, H.M.; Chen, X.Y. Er³⁺-doped anatase TiO₂ nanocrystals: Crystal-field levels, excited-state dynamics, up conversion, and defect luminescence. *Small* **2011**, *7*, 3046–3056.
10. Hafez, H.; Saif, M.; Abdel-Mottaleb, M.S.A. Down-converting lanthanide doped TiO₂ photoelectrodes for efficiency enhancement of dye-sensitized solar cells. *J. Power. Sources.* **2011**, *196*, 5792–5796.
11. Zhu, J.F.; Deng, Z.G.; Chen, F.; Zhang, J.L.; Chen, H.J.; Anpo, M.; Huang, J.Z.; Zhang, L.Z. Hydrothermal doping method for preparation of Cr³⁺-TiO₂ photocatalysts with concentration gradient distribution of Cr³⁺. *Appl. Catal. B* **2006**, *62*, 329–335.
12. Cha, W.; Le, H.A.; Chin, S.; Kim, M.; Jung, H.; Yun, S.T.; Jurng, J. Enhanced low-temperature NH₃-SCR activity of a V₂O₅/TiO₂ composite prepared via chemical vapor condensation and impregnation method. *Mater. Res. Bull.* **2013**, *48*, 4415–4418.
13. Janisch, R.; Gopal, P.; Spaldin, N.A. Transition metal-doped TiO₂ and ZnO-present status of the f field. *J. Phys. Condens. Matter.* **2005**, *17*, R657–R689.
14. Li, Y.Z.; Jin, S.F.; Xie, H.; Chen, X.; Tian, T.T.; Zhao, X.J. Highly selective photocatalytic and sensing properties of 2D—Ordered dome of nano-titania and nano-Ag²⁺ doped titania. *J. Mater. Chem.* **2012**, *22*, 1469–1476.
15. Liu, L.C.; Gu, X.R.; Sun, C.Z.; Li, H.; Deng, Y.; Gao, F.; Dong, L. *In situ* loading of ultra-small Cu₂O particles on TiO₂ nanosheets to enhance the visible-light photoactivity. *Nanoscale* **2012**, *4*, 6351–6359.
16. Navio, J.; Colon, G.; Trillas, M.; Peral, J.; Domenech, X.; Testa, J.J.; Padron, J.; Rodriguez, D.; Litter, M.I. Heterogeneous photocatalytic reactions of nitrite oxidation and Cr(VI) reduction on iron-doped titania prepared by the wet impregnation method. *Appl. Catal. B* **1998**, *16*, 187–195.
17. Ranjit, K.T.; Viswanthan, B.; Photochem, J. Synthesis, characterization and photocatalytic properties of iron-doped TiO₂. *Catalysts. Photobiol. B* **1997**, *108*, 79–84.
18. Yoshida, M.; Prasad, P.N. Sol-gel-processed SiO₂/TiO₂/poly(vinylpyrrolidone) composite materials for optical waveguides. *Chem. Mater.* **1996**, *8*, 235–241.
19. Tatsuma, T.; Saitoh, S.; Ohko, Y.; Fujishima, A. TiO₂-WO₃ photoelectro chemical anticorrosion system with an energy storage ability. *Chem. Mater.* **2001**, *13*, 2838–2842.
20. Huang, J.; Shinohara, T.; Tsujikawa, S. Effects of interfacial iron oxides on corrosion protection of carbon steel by TiO₂ illumination. *Zairyo-to-Kankyo* **1997**, *469*, 651–661.
21. Chen, F.; Xie, Y.D.; Zhao, J.C.; Lu, G.X. Photocatalytic degradation of dyes on a magnetically separated photocatalyst under visible and UV irradiation. *Chemosphere* **2001**, *44*, 1159–1168.
22. Xu, S.H.; Shangguan, W.F.; Yuan, J.; Chen, M.X.; Shi, J.W. Synthesis and performance of novel magnetically separable nanospheres of titanium dioxide photocatalyst with egg-like structure. *Appl. Catal. B* **2007**, *71*, 177–184.
23. Aziz, A.A.; Cheng, C.K.; Ibrahim, S.; Matheswaran, M.; Saravanan, P. Visible light improved, photocatalytic activity of magnetically separable titania nanocomposite. *Chem. Eng. J.* **2012**, *183*, 349–356.

24. Yang, Y.; Guo, Y.H.; Hu, C.W.; Wang, Y.H.; Wang, E.B. Preparation of surface modifications of mesoporous titania with monosubstituted Keggin units and their catalytic performance for organochlorine pesticide and dyes under UV irradiation. *Appl. Catal. A* **2004**, *273*, 201–210.
25. Li, Y.X.; Zhang, M.; Guo, M.; Wang, X.D. Preparation and properties of a nano TiO₂/Fe₃O₄ composite superparamagnetic photocatalyst. *Rare Metals* **2009**, *28*, 423–427.
26. Das, S.K.; Bhunia, M.K.; Haumik, A.B. Self-assembled TiO₂ nanoparticles: Mesoporosity, optical and catalytic properties. *Dalton Trans.* **2010**, *39*, 4382–4390.
27. Zhang, Y.; Yu, X.; Jia, Y.; Jin, Z.; Liu, J.H.; Huang, X.J. A facile approach for the synthesis of Ag-coated Fe₃O₄@TiO₂ core/shell microspheres as highly efficient and recyclable photocatalysts. *Eur. J. Inorg. Chem.* **2011**, *2011*, 5096–5104.
28. Cullity, B.D.; Stock, S.R. *Elements of X-ray Diffraction*; Prentice Hall: Upper Saddle River, NJ, USA, 2001; pp. 385–433.
29. Chen, C.T.; Chen, Y.C. Fe₃O₄/TiO₂ core/shell nanoparticles as affinity probes for the analysis of phosphopeptides using TiO₂ surface-assisted laser desorption/ionization mass spectrometry. *Anal. Chem.* **2005**, *77*, 5912–5919.
30. Yeh, C.S.; Wu, M.T.; Shieh, D.B.; Cheng, F.Y.; Su, C.H.; Yang, Y.S.; Tsai, C.Y. Characterization of aqueous dispersions of Fe₃O₄ nanoparticles and their biomedical applications. *Biomaterials* **2005**, *26*, 729–738.
31. Li, Y.; Wu, J.S.; Qi, D.W.; Xu, X.Q.; Deng, C.H.; Yang, P.Y.; Zhang, X.M. Novel approach for the synthesis of Fe₃O₄@TiO₂ core–shell microspheres and their application to the highly specific capture of phosphopeptides for MALDI-TOF MS analysis. *Chem. Commun.* **2008**, *5*, 564–566.
32. Hao, R.; Xing, R.J.; Xu, Z.C.; Hou, Y.L.; Sun, S.H.; Gao, S. Synthesis, functionalization, and biomedical applications of multifunctional magnetic. *Adv. Mater.* **2010**, *22*, 2729–2742.
33. Zanjianchi, M.A.; Noei, H.; Moghimia, M. Rapid determination of aluminum by UV-vis diffuse reflectance spectroscopy with application of suitable adsorbents. *Talanta* **2006**, *70*, 933–939.
34. Yang, Y.; Hu, C.W.; Wu, Q.Y.; Guo, Y.H.; Wang, E. Efficient degradation of dye pollutants on nanoporous polyoxotungstate–anatase composite under visible-light irradiation. *J. Mol. Catal. A Chem.* **2005**, *225*, 203–212.
35. Asahi, R.; Morikawa, T.; Ohwaki, T.; Aoki, K.; Taga, Y. Visible-light photocatalysis in nitrogen-doped titanium oxides. *Science* **2001**, *293*, 269–271.
36. Kumar, N.; Maitra, U.; Hegde, V.I.; Waghmare, U.V.; Sundaresan, A.; Rao, C.N.R. Synthesis, characterization, photocatalysis, and varied properties of TiO₂ cosubstituted with nitrogen and fluorine. *Inorg. Chem.* **2013**, *52*, 10512–10519.
37. Khataee, A.R.; Zarei, M.; Moradkhannejhad, L.; Nourie, S.; Vahid, B. Nitrogen doping of commercial TiO₂ nanoparticles for enhanced photocatalytic degradation of dye under visible light: Central composite design approach. *Adv. Chem. Lett.* **2013**, *1*, 24–31.